Dynamics of entrapped microbubbles with multiple openings

Amit Dolev*, Murat Kaynak, Mahmut Selman Sakar
Institute of Mechanical Engineering, École Polytechnique Fédérale de Lausanne, CH-1015 Lausanne, Switzerland

*Corresponding author

E-mail address: amitdtechnion@gmail.com

Postal address: MED 3 2715 (Bâtiment MED) Station 9 CH-1015 Lausanne, Switzerland

Author e-mail addresses:

Murat Kaynak: murat.kaynak@epfl.ch

Mahmut Selman Sakar: selman.sakar@epfl.ch

ABSTRACT

Microbubbles excited by acoustic fields inside water oscillate, and generate acoustic radiation forces and drag-induced acoustic streaming. These forces can be harnessed in various biomedical applications such as targeted drug delivery and on-chip biomanipulation. The conventional approach for using microbubbles as actuators is to trap them inside microfabricated cavities. Anisotropic forces are applied by constraining the interfaces where the air interacts with water. The existing analytical models derived for spherical bubbles are incapable of predicting the dynamics of bubbles in such configurations. Here, a new model for bubbles entrapped inside arbitrarily shaped cavities with multiple circular openings is developed. The semi-analytical model captures a more realistic geometry through a solution to an optimization problem. We challenge the assumption that bubbles should be excited at their first resonance frequency to optimize their performance. The natural frequencies and the correlated normal vibration modes are calculated, which are subsequently used to compute the acoustic streaming patterns and the associated thrust by a finite element simulation. An experimental platform was built to measure the deflection of beams loaded by microfabricated bubble actuators, and visualize the generated streaming patterns. The results highlight the contribution of the computational model as a design tool for engineering applications.

I. INTRODUCTION

Microbubbles trapped inside microcavities engraved on the walls of microfluidic devices have been used as wireless actuators for on-chip manipulation of particles, cells, and entire organisms[1,2]. Likewise,

microbubbles encapsulated within untethered structures serve as propellers for mobile micromachines[3–5]. In an acoustic field, entrapped microbubbles oscillate and generate two different types of forces: drag-induced microstreaming (i.e., confined mean flow[6,7]) and radiation forces[8]. It has been widely accepted that microbubbles deliver the best performance when the acoustic field is tuned to the resonance frequency of the microbubble[3,4,9–12]. As a manifestation of this assumption, experimental studies reported the frequency at which the velocity of the surrounding fluid or bubble-propelled machine peaked as the resonance frequency of the microbubble. However, the reported results may be misleading because the properties of the driving acoustic signal (e.g., the pressure generated by the transducer) have been ignored or not fully characterized. Furthermore, directly measuring the displacement at the surface of the microbubble at different excitation frequencies is very challenging, particularly when the bubble is not stationary, because the bubble deformation occurs in 3D and the vibration amplitude is up to a few microns[5,11,13,14]. Optimizing the performance of microbubble actuators is essential for the development of next-generation biomedical devices and untethered microrobots[15,16].

A complete understanding of microbubble dynamics involves the calculation of vibration modes, corresponding natural frequencies, and generated thrust due to acoustic streaming (AS). Theoretical work has been focused on basic configurations—free bubbles with a spherical geometry[8,17,18]. The formulation involves an analytical approximation for the natural frequencies and associated vibration modes. Notable examples are models of gas bubbles in inviscid fluids[17,19,20], viscous fluids[21,22], yield-stress fluids[23], viscoelastic fluids[24], liquid confined in elastic solids[25], bubbles encapsulated by a viscoelastic shell[26] and lipid coated bubbles[27]. In addition, Maksimova studied the effects of boundaries on the bubble's oscillations[28]. The case of entrapped bubbles with a single opening or multiple openings attracted less attention. The early work by Miller and Nyborg provides an approximation for the first resonance frequency of a cylindrical gas-filled pore on an infinite surface[29]. The governing equation was derived by assuming a parabolic vibration mode. Gelderblom *et al.*, extended the model presented in[29] to include axisymmetric vibration modes by solving fluid-gas coupled problems[30]. The gas was modeled as an ideal gas while the fluid was modeled using potential flow in the lossless case and unsteady stokes flow in the lossy case. Gritsenko *et al.* studied the natural frequencies and general vibration modes (i.e., axisymmetric and non-axisymmetric) of baffled cylindrical gas-filled pores

assuming the gas-fluid interface was clamped[31]. Notably, the coupled gas and fluid fields were modeled differently, using velocity potentials, following the work by Chindam *et al.*,[32]. Schnitzer *et al.*, systematically studied bubbles trapped in microgrooves, considering their resonance frequencies and acoustic interactions[33]. The gas and fluid fields were modeled using acoustic equations, namely, Helmholtz equations because the primary objective was to study acoustic phenomena. Spelman *et al.*, studied entrapped spherical bubbles with multiple openings[10]. Their formulation was based on the analysis of fluid immersed spherical gas bubbles with constraints[34]. Harazi *et al*.[35] developed a simplified analytical model of mesoscale cubic bubbles and experimentally validated model predictions. Boughzala *et al.*[36] extended the model to the general case of polyhedral bubbles. In both studies, the researchers studied the first resonance frequency and showed that the system can be approximated with the Minnaert model[37].

Radiation forces and AS generated by vibrating bubbles are nonlinear phenomena that can seldom be formulated and solved analytically. Therefore, they have been calculated numerically by employing various methods including finite element method (FEM), boundary element method (BEM), and computational fluid dynamics (CFD). The research in this domain has been focused on the primary forces acting on particles and bubbles in acoustic fields, and not on the secondary forces generated by the excited structures. These secondary effects give rise to additional radiation forces and AS, which are proven to be effective in micromanipulation. Although knowing the streaming patterns and thrust generated by the secondary fields is important, to our knowledge, they have not been correlated to the vibration modes of entrapped microbubbles. Volk and Kähler[11] investigated the influence of bubble size on streaming patterns, yet, the results were not correlated to the vibration modes. The primary forces which are due to the primary fields can be computed for various geometries using different methods. Dolev *et al.*, computed the acoustic field using BEM and then employed Gor'kov's theory to estimate the acoustic radiation forces acting on an acoustically levitated rigid sphere[38]. Muller *et al.*, provided FEM-based methodology to calculate both the acoustic radiation force and AS induced drag force acting on small particles[39]. Their methodology was built upon the perturbation solution of the thermoacoustic equations. Behdani *et al.* studied the streaming patterns generated by the oscillation of a microbubble in a microfluidic channel by a direct numerical simulation – CFD[40].

In this paper, we study the acoustic excitation of entrapped gas microbubbles with multiple openings, the streaming patterns, and generated thrust. We focus on natural frequencies and not resonance frequencies for three reasons. First of all, radiation forces and AS are acoustic phenomena that are driven by the gas-fluid interface velocity while the maximum velocities are obtained at the natural frequencies[41]. Second, the natural frequencies and normal modes are independent of the damping in the systems and, thus, can be treated as inherent characteristics of the linear system. Lastly, as demonstrated by Gelderblom *et al.*,[30], resonance frequencies of a gas pocket can be reliably predicted by the potential flow model (i.e., lossless). Regarding the last point, when using modal analysis, the relation between the resonance frequency and natural frequency is

$$\omega_r = \omega_n \sqrt{1-2\zeta^2}\,, \tag{1}$$

where ω_r is the resonance frequency, ω_n is the natural frequency, and ζ is the modal damping. Following Eq.(1), $\omega_r \approx \omega_n$ when the damping is low (i.e., almost lossless). To solve the natural frequencies and vibration modes for the general case, which involves multiple openings and a finite surface, a semi-analytical method is proposed. The method is based on an optimization problem that couples the analytical solutions with a BEM simulation. Once the natural frequencies and vibration modes are estimated, the solution is used in a FEM simulation to compute the streaming patterns and generated thrust[39,42]. The numerical results showed that different vibration modes generate different streaming patterns and that the thrust is highly dependent on the excitation frequency. On one hand, higher frequencies lead to stronger thrust, but on the other hand, higher modes generate weaker thrust.

To verify the assumptions of the model and validate the simulation results, experiments were carried out using a platform comprising a water tank, a hydrophone, an imaging system, and a computer-controlled ultrasonic transducer. The tank was placed on top of an inverted microscope to which a high-speed camera was mounted. We performed experiments on microfabricated polymer devices encapsulating microbubbles with two openings. The high-speed camera recorded the streaming patterns and the deflection of the structures. The results show that different modes were excited.

The rest of the paper is organized as follows. In Section II, we derive the governing equations of a trapped bubble with multiple openings. In Section III, we introduce the coupled optimization problem. FEM

simulations for the computation of the streaming patterns and thrust are described in Section IV. The same section contains a sensitivity analysis for the model parameters. In Section V, a microdevice entrapping a bubble with two openings is studied. Its governing equations of motion including damping and external forcing are provided. The theoretical analysis is verified experimentally, demonstrating the ability to excite different modes. Finally, we present the conclusions from the study in Section VI.

II. NATURAL FREQUENCIES AND VIBRATION MODES – EXTREME CASES

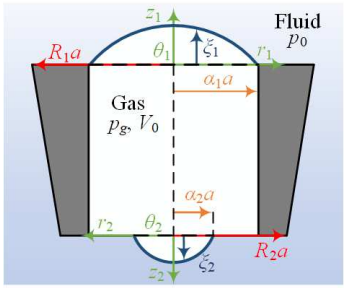

Fig. 1. The geometry of the problem. A gas-filled cavity with two interfaces immersed in a fluid. The solid walls entrapping the bubble are denoted with black contour, the solid is colored grey, and the gas-fluid interfaces are highlighted with blue lines. The local coordinate systems are sketched in green, and the dimensions are given in orange and red.

A. GOVERNING EQUATIONS OF MOTION

The complete problem is complex and includes multiple physical phenomena such as the thermal behavior inside the bubble[43,44], the interior gas dynamics[45], and the contact angle at the edge of the interface[11,30,35,36]. To derive the governing equations for the lossless case of a fluid-immersed entrapped gas bubble with multiple openings, we follow the work and assumptions of Gelderblom *et al.*[30]. The gas is assumed ideal, and the fluid domain is modeled assuming potential flow. To simplify the math, we derive the equations for a cavity with two interfaces as shown in Fig. 1.

The complete list of modeling assumptions is as follows:

1) The cavity has circular openings.
2) The interface is pinned to the circular edge of the cavity.
3) The surrounding fluid is incompressible and inviscid.

4) The interface is flat at the equilibrium.

5) There are no loss mechanisms neither in the gas nor in the fluid..

6) The gas flow within the cavity is negligible.

7) Linear harmonic analysis can be used to analyze the coupled problem.

8) The process in the gas can be modeled as Polytropic..

9) There is no interaction between the interfaces through the liquid.

10) The acoustic wavelength in the cavity is much larger than the size of the cavity.

The local deflection of each interface is described by $\xi_i(r_i, \theta_i, t)$, i = 1,2, with a local cylindrical coordinate system located on the axis of each cavity's opening. Employing lossless harmonic analysis, the interfaces can be described as:

$$\xi_i(r_i,\theta_i,t) = \xi_i(r_i,\theta_i)\mathrm{e}^{j\omega t}, \quad j=\sqrt{-1}\,. \tag{2}$$

Each interface motion is coupled to the velocity field in the liquid through a kinematic condition that yields:

$$u_{iz} = j\omega\xi_i\,, \tag{3}$$

here, $\mathbf{u}_i = u_{ir}\hat{\mathbf{r}} + u_{iz}\hat{\mathbf{z}}$ is the velocity field in the fluid near the opening i.

The boundary conditions for the fluid domain are as follows:

On the interface, due to assumption 4, and the kinematic condition:

$$u_{iz}\big|_{z_i=0} = j\omega\xi_i, \quad 0 \le r_i/a \le \alpha_i\,. \tag{4}$$

On the solid surface (z_i=0), no penetration and no-slip conditions are denoted as:

$$u_{iz}\big|_{z_i=0} = 0, \quad \alpha_i \le r_i/a \le R_i\,, \tag{5}$$

$$u_{ir}\big|_{z_i=0} = 0, \quad \alpha_i \le r_i/a \le R_i\,. \tag{6}$$

We ignore the boundary conditions on the cavity walls. The coupling between the pressures in the liquid and the gas occurs via the dynamic boundary conditions at z_i=0.

$$p_g = p_i + \sigma C_i - 2\mu \left. \frac{\partial u_{iz}}{\partial z_i} \right|_{z_i=0} . \tag{7}$$

Here, p_g is the pressure in the gas bubble, p_i is the pressure in the liquid adjacent to the i^{th} interface, σ is the surface tension coefficient, C_i is the curvature of the free surfaces ξ_i, and μ is the fluid's dynamic viscosity. As a result of assumption 3, μ is neglected. Considering small deflections, the curvature for the free surfaces is approximated by

$$\mathrm{C}_i \approx -\left(\frac{1}{r_i}\frac{\partial \xi_i}{\partial r_i} + \frac{\partial^2 \xi_i}{\partial r_i^2} + \frac{1}{r_i^2}\frac{\partial^2 \xi_i}{\partial \theta_i^2} \right). \tag{8}$$

We assume a general polytropic relation between the instantaneous gas volume V and the gas pressure p_g. Expanding the relation for small volume variations yields

$$p_g = p_0 \left(\frac{V_0}{V} \right)^{\kappa} \approx p_0 \left[1 - \kappa \left(\frac{V}{V_0} - 1 \right) \right], \tag{9}$$

where V_0 is the cavity's volume when the interfaces are flat, κ is the gas polytropic index, and κ=1 is applicable for isothermal conditions. The instantaneous gas volume can be found from the shape of the interfaces by the following integration:

$$\begin{aligned} V &= V_0 \left(1 + \sum_i \frac{a^3}{V_0} \frac{\int_0^{2\pi} \int_0^{a\alpha_i} \xi_i(r_i, \theta_i, t) r_i dr_i d\theta_i}{a^3} \right) = V_0 \left(1 + \lambda \sum_i \frac{H_i}{a^3} \right), \\ H_i &= \int_0^{2\pi} \int_0^{a\alpha_i} \xi_i(r_i, \theta_i, t) r_i dr_i d\theta_i, \quad \lambda = \frac{a^3}{V_0}. \end{aligned} \tag{10}$$

Substituting Eqs.(9)-(10) to Eq. (7), the dynamic boundary condition becomes

$$p_0 \left(1 - \kappa\lambda \sum_i \frac{H_i}{a^3} \right) = p_i - \sigma \left(\frac{1}{r_i}\frac{\partial \xi_i}{\partial r_i} + \frac{\partial^2 \xi_i}{\partial r_i^2} + \frac{1}{r_i^2}\frac{\partial^2 \xi_i}{\partial \theta_i^2} \right). \tag{11}$$

From Eq.(11) and assumptions 1 and 2, it is intuitive to select the vibration modes of a circular membrane as basis functions for spanning the vibration modes.

According to assumption 3, the flow is irrotational, and the velocity field can be written in terms of a velocity potential. Moreover, due to assumption 9, the velocity fields near each opening are assumed to be local, and thereby can be described by local potentials as follows:

$$\mathbf{u}_i = \nabla \phi_i. \tag{12}$$

The following dimensionless quantities are used from here forth without the hat symbol $\hat{\bullet}$.

$$\hat{r}_i = \frac{r_i}{a}, \quad \hat{z}_i = \frac{z_i}{a}, \quad \hat{\xi}_i = \frac{\xi_i}{a}, \quad \hat{u}_i = \sqrt{\frac{a\rho}{\sigma}} u_i, \quad \hat{\phi}_i = \sqrt{\frac{\rho}{a\sigma}} \phi, \quad \hat{t} = \sqrt{\frac{\sigma}{a^3 \rho}} t, \quad \hat{p}_i = \frac{a}{\sigma} p_i, \quad \hat{H}_i = \frac{H_i}{a^3}. \tag{13}$$

B. POTENTIAL AND KINETIC ENERGIES

The system is considered lossless and Lagrange equations can be employed to derive the governing equations.

$$\frac{d}{dt}\left(\frac{\partial \mathrm{L}}{\partial \dot{q}_l}\right) - \frac{\partial \mathrm{L}}{\partial q_l} = 0, \quad l = 1, 2, ..., \quad \mathrm{L} = \mathrm{E}_k - \mathrm{E}_p \tag{14}$$

where the overdot $\dot{\bullet}$ indicates a derivative with respect to time t, $\mathbf{q}$ is a set of generalized degrees of freedom (DOF), L, E_k and E_p are the Lagrangian, kinetic energy, and potential energy of the system, respectively. The contribution of the irrotational flow near each interface to the kinetic energy is expressed as[46]:

$$\mathrm{E}_{ki} = \frac{1}{2} \int_A \phi_i \frac{\partial \phi_i}{\partial \hat{\mathbf{n}}} dA, \tag{15}$$

where $\hat{\mathbf{n}}$ is a unit vector pointing out of the fluid. Far from the interfaces, the velocity reduces to zero. The impermeability conditions imply that the total kinetic energy is given by

$$\mathrm{E}_k = \sum_i \mathrm{E}_{ki}, \quad \mathrm{E}_{ki} = -\frac{1}{2} \int_0^{2\pi} \int_0^{\alpha_i} \phi_i \big|_{z_i = 0} \frac{\partial \xi_i}{\partial t} r_i dr_i d\theta_i. \tag{16}$$

The potential energy of the system is related to the surface tension and the volume of the microbubble. The energy increases when the area of the interface grows and the bubble volume decreases.

$$\mathrm{E}_p = \sum_i \int_{A_{i0}}^{A_i} dA_i - \int_{V_0}^{V} \left(p_g - p_0 \right) dV. \tag{17}$$

Substituting Eq.(9) and assuming small amplitude variations, the potential energy is approximated as

$$\mathrm{E}_p \approx \frac{1}{2} \sum_i \int_0^{2\pi} \int_0^{\alpha_i} \frac{1}{r_i} \left(\frac{\partial \xi_i}{\partial \theta_i} \right)^2 + r_i \left(\frac{\partial \xi_i}{\partial r_i} \right)^2 dr_i d\theta_i + \frac{\kappa \lambda p_0}{2} \sum_i \sum_j H_i H_j. \tag{18}$$

To solve the general problem for which $0 < R_i \leq \infty$, we first solve for two extreme cases, free (R_i=0) and baffled (R_i=∞). Notice that the free case is not physical.

1. THE FREE BUBBLE

To solve the interface displacement fields, we span them using a set of basis functions. As mentioned in Section A, these functions are essentially the vibration modes of a circular membrane[47].

$$\xi_i \left(r_i, \theta_i, t \right) = \sum_{m=0}^{\infty} \sum_{n=1}^{\infty} J_m \left(j_{mn} \frac{r_i}{\alpha_i} \right) \left[q_{imnA} \cos\left(m\theta_i \right) + q_{imnB} \sin\left(m\theta_i \right) \right], \quad m = 0,1,... \quad n = 1,2,... \tag{19}$$

Here, J_m is a Bessel function of the first kind of order m, j_{mn} is the n^{th} zero of J_m, and q_{imnA} and q_{imnB} are time-dependent unknown functions. Because the potential energy depends only on the gas bubble, substituting Eq.(19) into Eq.(18) yields Eq.(A1). In the free bubble case, the only boundary condition to be satisfied is given by Eq.(4), and the following potential fields are assumed[31]

$$\phi_i^{(F)} \left(r_i, \theta_i, z_i, t \right) = -\sum_{m=0}^{\infty} \sum_{n=1}^{\infty} \frac{1}{j_{mn}} J_m \left(j_{mn} \frac{r_i}{\alpha_i} \right) \left[\dot{a}_{imn} \cos\left(m\theta_i \right) + \dot{b}_{imn} \sin\left(m\theta_i \right) \right] \mathrm{e}^{-j_{mn} z_i}, \tag{20}$$

where a_{imn} and b_{imn} are time-dependent unknown functions. To compute a_{imn} and b_{imn}, the derivative of Eq.(20) with respect to z_i is computed. By using the boundary condition and the orthogonality properties of the trigonometric and Bessel functions, they are obtained as Eq.(A2). Substituting Eq.(A2) into Eq.(20), and the kinetic energy for a free bubble independent of a_{imn} and b_{imn} is obtained as Eq.(A3).

2. THE BAFFLED BUBBLE

We assume that the interface displacement fields can be spanned by the same basis functions as for the free bubble, and the boundary conditions to be satisfied are given by Eqs.(4) and (5). To satisfy them, the following potential fields are assumed[30]

$$\phi_i^{(B)}\left(r_i,\theta_i,z_i,t\right)=-\int_0^{\infty}\sum_{m=0}^{\infty}\Phi_{im}\left(k\right)J_m\left(k\frac{r_i}{\alpha_i}\right)\left[\dot{a}_{imn}\cos\left(m\theta_i\right)+\dot{b}_{imn}\sin\left(m\theta_i\right)\right]\mathrm{e}^{-kz_i}dk. \tag{21}$$

To compute a_{imn} and b_{imn} the derivative of Eq.(21) with respect to z_i is computed, then by using the boundary conditions and the orthogonality properties of the trigonometric and Bessel functions, they are obtained as Eq.(A4). Then, the kinetic energy for a baffled bubble is obtained as Eq.(A5).

3. THE INTERMEDIATE CASE

The intermediate case, where $R<\infty$, is a realistic situation that is more relevant to physical scenarios than the free and baffled cases. The potentials should comply with the boundary conditions given by Eqs.(4) and (6). However, no analytical potential satisfying these two conditions was found. We assume that the solution of the intermediate case lies in between the two extreme ones and introduced the following potential:

$$\phi_i^{(I)}=\mathrm{e}^{-\beta_i\left(R_i-\alpha_i\right)}\phi_i^{(F)}+\left(1-\mathrm{e}^{-\beta_i\left(R_i-\alpha_i\right)}\right)\phi_i^{(B)} \tag{22}$$

where β_i are unknown coefficients, which are found by solving an optimization problem as described in Section III.

C. DISCRETE LINEAR EQUATIONS OF MOTION

The problem is studied in the framework of linear harmonic analysis. It follows that every arbitrary time-dependent function can be described as $F(t) = Fe^{j\omega t}$. Notice that the frequency ω is normalized according to Eq.(13). Now, to discretize the continuous equations, the coefficient q_{imnA} and q_{imnB} are used as discrete DOF, indicating the participation factor of each basis function. Because the energies hold terms up to the second-order, utilizing the Lagrange equations yields discrete linear equations of motion. Similarly, we can directly derive the mass, **M**, and stiffness, **K**, matrices, and write the equations of motion as follows:

$$\mathbf{M}\ddot{\mathbf{q}}+\mathbf{K}\mathbf{q}=\mathbf{0} \tag{23}$$

The DOF in **q** can be re-arranged. Here, we use a finite set of cosine DOF (i.e., q_{imnA}), and order them as follows:

$$\begin{aligned}\mathbf{q} = \{&q_{101A} \quad q_{102A} \quad \cdots \quad q_{10NA} \quad q_{111A} \quad q_{112A} \quad \cdots \quad q_{11NA} \quad \cdots \quad q_{1M1A} \quad q_{1M2A} \quad \cdots \quad q_{1MNA} \quad \cdots \\ &q_{201A} \quad q_{202A} \quad \cdots \quad q_{20NA} \quad q_{211A} \quad q_{212A} \quad \cdots \quad q_{21NA} \quad q_{2M1A} \quad q_{2M2A} \quad \cdots \quad q_{2MNA}\}^T, \\ m = 0,1,2,...,M, \quad &n = 1,2,...,N\end{aligned} \tag{24}$$

We chose to use only the cosine DOF due to the problem's axisymmetric nature which yields doublet modes[48,49] (i.e., for each natural frequency where m>0 there is a cosine mode and a similar mode shifted in space by $\pi/2$, the sine mode). With this information, the stiffness and mass matrices can be computed (see Appendix B). It is visible from the topology of the matrices that the coupling between the openings is indeed only through the gas. Notably, only the axisymmetric functions of each opening (m=0) contribute to the coupling.

The potential given in Eq.(22) influences only the mass matrix (see Appendix B). Once the elements of **β** are calculated, as described in the following section, the stiffness and mass matrix can be computed. The generalized eigenproblem is then solved to compute the natural frequencies and the normal modes[41].

III. NATURAL FREQUENCIES AND VIBRATION MODES – INTERMEDIATE CASE

For the general case where the bubble lies on a finite plane, an additional parameter per each interface is required. To estimate these parameters, we devised an optimization problem that minimizes the error between the analytically and numerically obtained solutions as a function of **β**. From the analytical solution, we can obtain the natural frequencies, normal vibration modes, and potential fields. Moreover, because a potential flow is assumed, the analytical pressure field can be computed as follows:

$$p_i^{\mathrm{An}} = -j\omega\phi_i . \tag{25}$$

We assume a lossless harmonic problem; therefore, the pressure field can be computed numerically using a BEM simulation. The input to the simulation is the interface velocity, which is dictated by the analytically computed vibration modes and natural frequencies, and the output is the pressure field p_i^{BEM}. The intermediate case can be resolved by minimizing the error between the two fields:

$$\Delta = \sum_i \sqrt{\frac{\sum\left(p_i^{\mathrm{An}}(\mathbf{x}) - p_i^{\mathrm{BEM}}(\mathbf{x})\right)^2}{\sum\left(p_i^{\mathrm{BEM}}(\mathbf{x})\right)^2}}\,. \tag{26}$$

We compute the natural frequencies and matching normal modes for the free, baffled, and intermediate cases for several geometries. We begin by analyzing a bubble with a single opening and demonstrate the impact of the geometry and optimization procedure on the simulation results. The values for the model parameters are chosen as follows:

$$\begin{gathered}\sigma = 0.072\,\mathrm{N\,m^{-1}},\quad \kappa = 1.4,\quad \rho_{\mathrm{water}} = 998.24\,\mathrm{kg\,m^{-3}},\quad c_{\mathrm{water}} = 1481.4\,\mathrm{m\,s^{-1}},\\ p_0 = 101325\,\mathrm{Pa},\quad h = 150\,\mu\mathrm{m},\quad a = 20\,\mu\mathrm{m},\quad R = 1.1.\end{gathered} \tag{27}$$

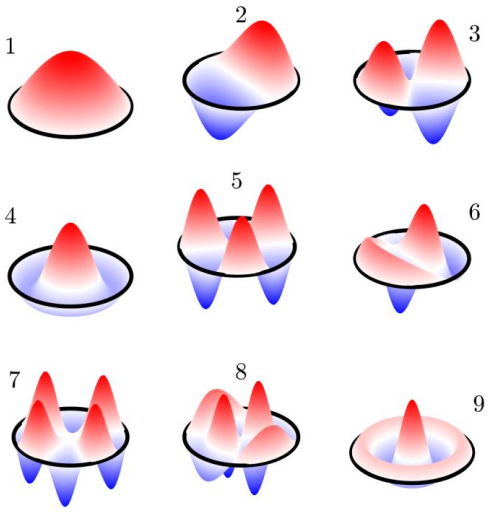

Fig. 2. The first nine analytically computed normal vibration modes of the baffled bubble. Modes 1, 4, and 9 are axisymmetric, while the rest are not. For each non-axisymmetric mode, there should be a similar mode shifted in space by $\pi/2$ having the same natural frequency.

We reduced the computation time while maintaining a sufficient level of accuracy by truncating the basis function series and selecting M=4 and N=3, following a convergence analysis. The truncated series provided accurate predictions of all the modes up to the third axisymmetric mode. The mode shapes of the baffled case are shown in Fig. 2 which are almost identical to the mode shapes of the free case.

We are interested in finding the solution for the intermediate case when R is finite. To this end, the optimization problem that was described in Section III is solved using MATLAB's built-in functions from the Optimization and Global Optimization Toolboxes. The acoustic field is simulated using OpenBEM[50] according to the selected mode(s), where the input to each simulation is the interface velocity obtained from the modal analysis. By minimizing the error, the optimal value for $\boldsymbol{\beta}$ is calculated. In general, the obtained results show that the optimization scheme leads to an accurate estimation of the pressure fields by the analytical model. The natural frequencies for the three different cases are given in Table 1. The natural frequencies were computed using two optimization schemes. In the first, each mode was estimated separately (i.e., each mode yielded a different value for β). In the second scheme, all the considered modes were computed together (i.e., yielding a single value for β). The results highlight the importance of considering the geometry near the opening of the microbubble. Although the mode shapes are practically identical, the relative error between the computed natural frequencies for the extreme cases can be higher than 33% for the first mode. The relative error reduces below 10% for higher modes, nevertheless, the difference remains more than 10 kHz. Notably, the intermediate solution lies in between the two extreme cases, and as R increases, the solution approaches the baffled solution as expected. The latter can be rationalized as follows; larger R increases the flow resistance, thus increasing the inertia, which results in lower natural frequencies. We can conclude that the optimization scheme (single mode versus all modes) has a negligible effect on the results, as the maximum obtained relative error is 1.32%. In practice, the uncertainty in the values of the parameters is expected to lead to larger errors.

Table 1 Computed natural frequencies for a bubble with a single opening

Mode		1	3	4	8	9
Baffled (kHz)		53.65	162.86	175.26	349.95	360.36
Free (kHz)		71.51	175.87	198.31	369.04	385.44
R = 1.1	Single mode (kHz)	57.33	163.85	178.57	351.65	363.48
	All modes (kHz)	57.01	166.01	178.54	354.06	363.51
	R.E. (%)	0.56	1.32	0.02	0.69	0.01
R = 2	Single mode (kHz)	55.56	162.86	176.67	350.02	361.58
	All modes (kHz)	55.10	164.27	176.64	351.76	361.68
	R.E. (%)	0.83	0.87	0.02	0.50	0.03
R = 3	Single mode (kHz)	54.90	162.86	176.14	349.95	361.11
	All modes (kHz)	54.58	163.78	176.14	351.12	361.20
	R.E. (%)	0.58	0.56	0.00	0.33	0.02

Following a similar procedure, the natural frequencies and vibration modes of an entrapped bubble with two openings were computed. The first nine vibration modes for the baffled case with the following parameters $\alpha_1 = 1$, $\alpha_2 = 0.6$ (see Eq.(27) and Fig. 1, the opening radii are 20 μm and 12 μm) are shown in Fig. 3. As for a bubble with a single opening, the mode shapes dependency on R is negligible and they resemble, however, the natural frequencies vary considerably as shown in Table 2. For the selected parameters, both interfaces are deformed only in the first two modes, and at higher modes, only one is deformed. This characteristic can be

Table 2 Computed natural frequencies for a bubble with two openings

Mode		1	2	3	5	6
Baffled (kHz)		51.95	79.78	100.39	167.31	175.04
Free (kHz)		69.42	96.97	113.34	188.91	198.35
$R_1 = 1.1$ $R_2 = 1.1$	Single mode (kHz)	66.30	73.89	102.13	175.46	178.44
$R_1 = 1.1$ $R_2 = 2$	Single mode (kHz)	64.18	73.90	102.09	179.61	178.39
$R_1 = 1.1$ $R_2 = 3$	Single mode (kHz)	63.60	73.90	102.04	179.71	178.33

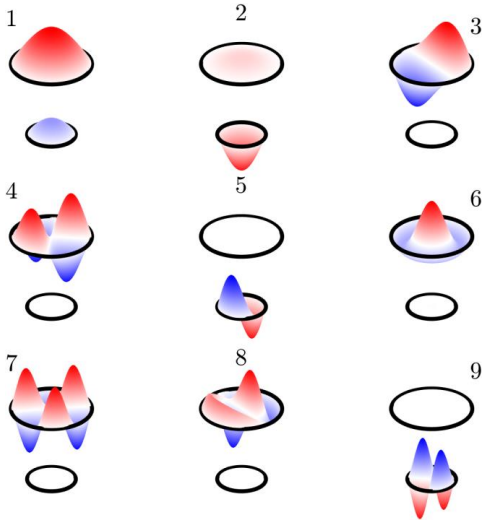

Fig. 3. The first nine analytically computed normal vibration modes assuming both interfaces are baffled, where the encapsulating structure is not shown for simplicity. The top opening is larger, and modes 1, 2, and 6 are axisymmetric, while the rest are not. For each non-axisymmetric there should be a similar mode shifted in space by $\pi/2$ having the same natural frequency. For modes 3 and higher, the deflection of one opening is negligible, and all the energy is concentrated in a single one.

used for frequency-selective actuation, where oscillations can be generated on both sides or at a single side. Each opening deformation shape can be correlated to the single opening bubble, and it is evident that the order for each opening is maintained (i.e., top opening modes 1, 3, 4, 6, 7, and 8 correlate to modes 1-6 in Fig. 2, and bottom opening modes 2, 5 and 9 correlate to modes 1-3 in Fig. 2).

When realizing this method, it is important to acknowledge the errors that may occur due to the discrepancies between the free and baffled bubble solutions, and related truncation errors. As mentioned in the introduction, commonly the first natural frequency is selected as the operational frequency. To compute it, the method assumes that in both extreme cases the mode shape is the same. However, this is not true for all geometries as can be seen in Fig. 4, which shows, for a single opening bubble, the two first natural frequencies of the extreme cases as a function of the bubble's radius. Beyond a≈48.5 μm for the baffled bubble and a≈56

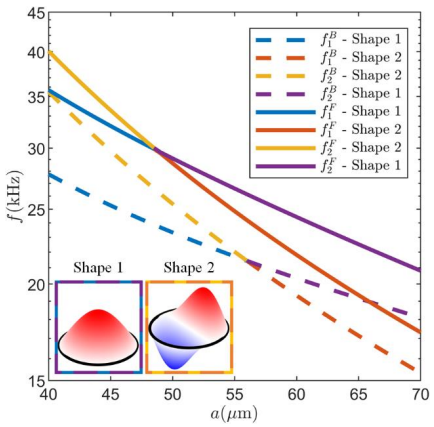

Fig. 4. The first two natural frequencies and matching vibrations modes shapes as a function of the bubble radius for the baffled (dashed lines) and free (continuous lines) cases. The two possible vibration mode shapes for both cases exchange their order for different values of the bubble radius.

μm for the free bubble, the mode shapes are different. Truncation of the basis function series may lead to similar results; therefore, it is important to perform a proper convergence analysis. Similar errors may also occur for higher natural frequencies. This observation was previously reported and justified by Gelderblom *et al.*, [30].

IV. ACOUSTIC STREAMING AND THRUST

We employed linear harmonic analysis to derive the modal characteristics of the system. The generated thrust and AS are nonlinear phenomena; therefore, cannot be directly computed with a linear model. For the latter, thermoviscous losses and higher-order terms should be considered. The losses give rise to the AS phenomenon by attenuating acoustic waves resulting in a transfer of pseudo-momentum from the wave to the fluid[39]. For the microbubbles, the dominating attenuation occurs at the boundaries due to the existence of a viscous boundary layer. By considering higher order terms, the thrust and AS can be approximated by time-averaging the stress acting on the bubble and the velocity field accordingly. The equations governing the thermoacoustic fields are well established, and the fields are usually written as perturbation series[51]:

$$\begin{aligned} T &= T_0 + T_1 + T_2, \\ p &= p_0 + p_1 + p_2, \\ \mathbf{v} &= \mathbf{v}_1 + \mathbf{v}_2, \end{aligned} \tag{28}$$

where T, p, and $\mathbf{v}$ denotes the temperature, pressure, and velocity fields, respectively. The subscript 0 represents the ambient conditions, where it is assumed that there is no mean flow. The subscript 1 and 2 represent the linear harmonic fields and the second-order nonlinear fields, respectively.

Due to the geometric complexity, a numerical approach is adopted here according to the work by Muller *et al.,*[39]. First, the harmonic acoustic thermoviscous problem is solved in COMSOL Multiphysics 5.5. Then, the obtained solution (i.e., p_1 and $\mathbf{v}_1$) is used to solve the second-order and time-averaged equations. The solution contains the time-averaged pressure field $\langle p_2 \rangle$ and velocity field $\langle \mathbf{v}_2 \rangle$, which are used to compute the streaming patterns and estimate the total force applied by the bubble (i.e., thrust) [42]:

$$\mathbf{F} = \int_{\partial\Omega} \left[\langle \sigma_2 \rangle - \rho_{water} \langle \mathbf{v}_1 \mathbf{v}_1 \rangle \right] \cdot \mathbf{n} da \,, \tag{29}$$

the angled brackets represent the time-average operator, $\partial\Omega$ is a static surface surrounding the bubble, σ_2 is the second-order stress field, and $\mathbf{n}$ is a surface vector into the fluid.

A. SENSITIVITY ANALYSIS

To perform sensitivity analysis we analyze the axisymmetric vibration modes of a bubble with a single opening. The first three axisymmetric modes for R = 1.1 are shown in Fig. 2. The procedure involves the analytical computation of the optimal solution for each mode separately. Next, the velocity distribution and the natural frequency for each mode were used as inputs to COMSOL to solve the thermosviscous problem and compute the second-order time-averaged fields. The velocity fields along with the streamlines are shown in Fig. 5. The streamlines for the various cases resemble, however, as higher vibration modes are considered the main vortex ring (highlighted in red in Fig. 5) changes and approaches the bubble's surface. Additional vortexes, which are also highlighted in red, are formed and the microjets emanating from the bubble's center become narrower (i.e., the radial distance to the vortex ring becomes smaller). Furthermore, higher velocities are obtained for higher vibration modes.

The generated thrust, which is defined as the net force in the z-direction, was computed numerically according to Eq.(29). The thrust increases with the frequency, and the natural frequencies decrease with increasing values of R and a. Therefore, to study the contribution of the mode shape alone (i.e., canceling the

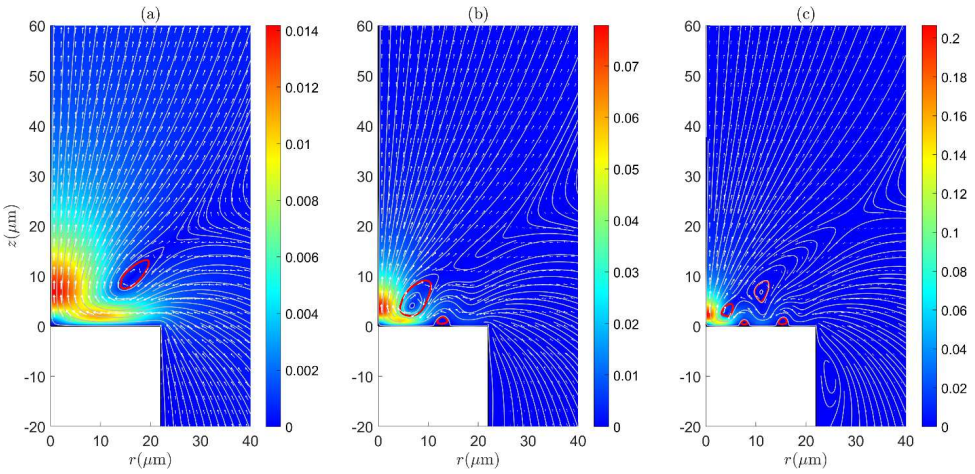

Fig. 5. The acoustic streaming patterns that are generated by the first three axisymmetric modes. The color map indicates the magnitude of the particle velocity $\left|\langle \mathbf{v}_2 \rangle\right|$ m s^{-1}, arrows indicate the direction, streamlines are shown in gray and some vortexes are highlighted in red. Panels (a), (b), and (c) correlate to modes 1, 4, and 9. The maximum displacement of the interface was set to 1 μm.

contribution of the frequency) to the thrust generation, we computed the stress for a maximum displacement of 1 μm (Fig. 6(a)) and maximum velocity of 0.1 m/s Fig. 6(b)). In the latter case, since the velocity is set, the excitation frequency cancels out. The computed thrust concerning R and a for the first three axisymmetric modes is shown in Fig. 6. For the fixed displacement case, higher modes generate more thrust and R has a negligible effect. Surprisingly, larger bubbles (i.e., larger a) generate less thrust in this scenario. In the second scenario, where constant velocity was used, lower modes and larger bubbles generate more thrust, as expected, while the influence of R remains negligible. The comparison between the two scenarios highlights the importance of the frequency and velocity as argued in the introduction (i.e., natural versus resonance frequencies). The thrust is highly dependent on the frequency, therefore lower modes and larger bubbles which have lower natural frequencies generate less thrust for the same displacement amplitude.

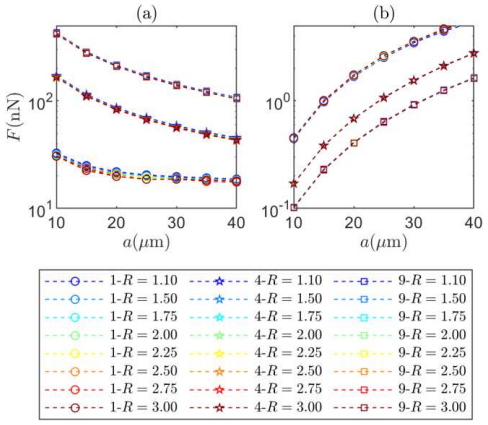

Fig. 6. The numerically computed thrust that is generated by a bubble with a single opening. The results are shown for the first three axisymmetric modes for various values of R, wherein (a) a maximum amplitude of 1 μm was used, and in (b) a maximum velocity of 0.1 m s^{-1} was used.

V. ENCAPSULATED MICROBUBBLE WITH TWO OPENINGS

In this section, we derive the governing equations of motion of an encapsulated bubble with two circular openings, as shown in Fig. 7. The capsule holding the bubble was 50 μm long, had an inner radius of 20 μm, an outer radius of 25 μm, and had two openings on both sides, with radii of 12 μm and 7 μm. We chose the dimensions such that the bubble can be treated as baffled, and that the first two natural frequencies are within

the frequency band of the water immersion transducer (see Fig. S4(b) in the Supplementary Material). Moreover, to stabilize the bubble we use saline water (25% salinity)[52,53]. The following parameters were used for the analysis.

$$\begin{gathered}\sigma = 0.079\,\mathrm{N\,m^{-1}}, \quad \kappa = 1.4, \quad \rho_{\mathrm{water}} = 1147.8\,\mathrm{kg\,m^{-3}}, \quad c_{\mathrm{water}} = 1776.1\,\mathrm{m\,s^{-1}}, \\ p_0 = 101325\,\mathrm{Pa}, \quad V_0 = 6.2832\times10^4\,\mu\mathrm{m}^3, \quad a = 12\,\mu\mathrm{m}, \\ \alpha_1 = 1, \qquad \alpha_2 = 7/12, \qquad R_1 = R_2 \to \infty.\end{gathered} \tag{30}$$

According to the chosen parameters, we computed the natural frequencies and vibration modes. The first two natural frequencies are 97.36 kHz and 153.46 kHz, and the matching vibration modes resemble the ones in Fig. 3. At these frequencies, the acoustic wavelength is much longer than the openings' diameter, even if one considers much higher frequencies (e.g., at 1 MHz, $\lambda \approx 1.5$ mm). As a result, we can treat the pressure wave

Fig. 7. Illustration of the capsule holding the bubble with a section cut for visualization.

impinging the bubble as uniform (see Supplementary Material) and we can easily project it on the basis functions and mode shapes through an inner product. To better approximate the system, losses which were overlooked thus far should be added to the model via modal damping. Estimating the modal damping coefficients is a challenging task because there are many loss mechanisms, such as acoustic radiation to infinity, losses in the gas and fluid, and heat conduction[8,43,54,55]. In general, the loss mechanisms are not linear as the bubble's dynamics[56,57]. However, considering the results obtained by Gelderblom *et al*.,[30] and the

parameters that are given in Eq.(30) we assume uniform modal damping of 20%. Now, the governing equations in modal coordinates[41] $\boldsymbol{\eta}$ are given by

$$\ddot{\boldsymbol{\eta}} + \boldsymbol{\Gamma}\dot{\boldsymbol{\eta}} + \boldsymbol{\Lambda}\boldsymbol{\eta} = \boldsymbol{\Phi}^{\mathrm{T}}\mathbf{Q}\,. \tag{31}$$

Here $\mathbf{I}$ is the identity matrix, $\boldsymbol{\Gamma}$ is the modal damping matrix, $\boldsymbol{\Lambda}$ is the modal stiffness matrix, $\boldsymbol{\Phi}$ is the modal matrix whose columns are the normal modes and $\mathbf{Q}$ is the uniform pressure projection on the basis functions. $\boldsymbol{\Gamma}$ is a diagonal matrix whose main entries are $2\zeta_i\omega_i$, and $\boldsymbol{\Lambda}$ is a diagonal matrix whose main entries are ω_i^2 where ζ_i and ω_i are the modal damping and natural frequency correlated to the i^{th} mode. For an impinging pressure wave with an amplitude of 0.5 kPa, the modal mobility plot for the first nine modes is shown in Fig. 8. A maximum displacement amplitude of around 1.4 μm is obtained at the center of the bigger opening. Only the axisymmetric modes (see modes 1, 2, and 6 in Fig. 3) are excited, and the first mode obtains the largest mobility at the associated natural frequency. The following axisymmetric modes also obtain large mobility values near their associated natural frequencies.

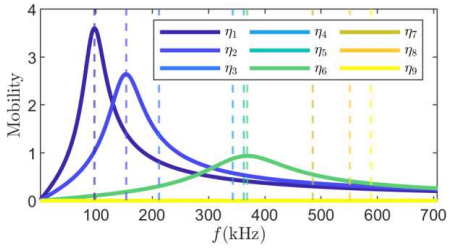

Fig. 8. Modal mobility plot, showing the first nine modes' response to a uniform pressure excitation, and dashed lines highlight the matching natural frequencies.

A. EXPERIMENTAL ESTIMATION OF THE NATURAL FREQUENCIES

The microstructures entrapping microbubbles with two openings were 3D printed using a two-photon polymerization technique (Nanoscribe Photonic Professional GT+, 3D laser writer), from a photopolymerizable polymer, IP-Dip, directly on a quartz glass substrate[58]. We closed a microfabricated Poly(dimethylsiloxane) (PDMS) microfluidic device around the structures to facilitate particle image velocimetry. Tracer particles (Polysciences - 1μm polystyrene microspheres) were injected into the microchannel to visualize the AS patterns, which were recorded by a high-speed camera (Phantom EVO640L).

A surfactant (TWEEN 20) was added to the saline water to avoid the tracer particles agglomeration. We fabricated only the capsule holding the bubble, as shown in Fig. 7. The microstructures were placed in a water tank atop an inverted microscope (Nikon Eclipse Ti-2-U). To excite the bubbles, a water immersion transducer (Ultran group, GPS100-D19) was used. The normalized spectrum of the transducer (see Fig. S4 in the Supplementary Material) was measured with a hydrophone (RP acoustics e.K. PVDF type s).

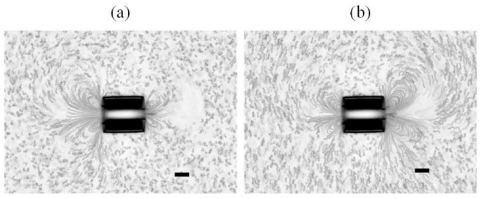

Fig. 9. The acoustic streaming patterns that were generated by an entrapped bubble with two openings at the same pressure amplitude of 0.25 kPa, and two frequencies. (a) At 71.2 kHz the dominant AS is near the large opening on the left, and (b) at 124.1 kHz the dominant AS is near the small opening on the right. Scale bars, 20 μm. Multimedia view

To estimate the natural frequencies, we did a frequency sweep and observed that AS was generated in a wide range of frequency bands. Yet, at certain bands, the AS was more dominant around one opening or the other. While frequencies close to 71.2 kHz, which corresponds to the first natural frequency of the bubble, generated a significantly stronger flow outside the larger opening, at frequencies close to 124.1 kHz, which corresponds to the second natural frequency of the bubble, the dominant AS was recorded around the smaller opening (Fig. 9 and video S9). The pressure amplitude was approximately 0.25 kPa at both frequencies. The discrepancy between the theoretical (97.36 kHz and 153.46 kHz) and empirical values of the natural frequencies may be due to various reasons, such as 3D printing inaccuracies, and errors in the fluid and gas parameters and the human factor. Experimental characterization of the optimal frequency via observation is not very accurate, especially considering the non-uniform spectrum of the transducer. Nevertheless, we were able to obtain the desired behavior where we can selectively excite each mode.

B. QUALITATIVE ESTIMATION OF THE THRUST

After a successful estimation of the natural frequencies, we wanted to qualitatively estimate the generated thrust. Using Eq.(31), we computed both interface velocity distribution in response to a uniform pressure field

of 0.5 kPa at different frequencies. Then, using COMSOL we computed the second-order stress and the total thrust with Eq.(29). The obtained results are shown in Fig. 10. It is noticeable that the force decreases and reaches its minimal value close to the first natural frequency. Then, as the frequency is increased it changes its sign and obtains its maximal value close to the second natural frequency. As the frequency is further increased, the thrust reduces and changes its sign again, and obtains a local minimum close to the sixth natural frequency. As the frequency is further increased, the thrust decays to zero. In general, the calculated force magnitude is in the same order as observed in previous works[59,60].

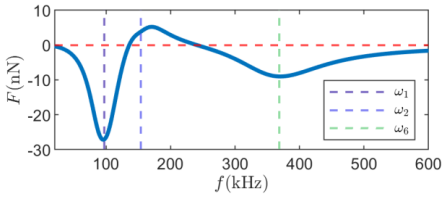

Fig. 10. Numerically computed thrust versus the excitation frequency for a pressure wave of 0.5 kPa. The dashed lines highlight the first, second, and sixth natural frequencies.

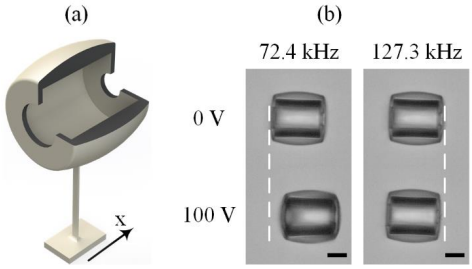

Fig. 11. (a) Illustration of the capsule holding the device attached to an upright cantilever beam with a section cut for visualization. (b) Bright-field microscopy images of the same device when it is not actuated (top images) and when it is actuated at two different frequencies, scale bar 20 μm.

Direct measurement of the thrust requires a force sensor with piconewton resolution. Moreover, the microstructures should be attached to the sensor, which is a challenging task. To circumvent the latter, we 3D printed flexible cantilever beams (56 μm long with a cross-section of 1.25 μm by 3.75 μm) from a biocompatible soft polymer, trimethylolpropane ethoxylate triacrylate (TPETA)[61]. The bubble actuator was attached to the end of the cantilever, as shown in Fig. 11(a). We focused on the first two natural frequencies

to reduce the complexity due to the rich spectrum of the transducer (Fig. S4). Following a similar procedure as in Section A, the first two natural frequencies were estimated as 72.4 kHz and 127.3 kHz. Then, the bubble was excited at different input voltage amplitudes, while the deformation at the tip was tracked, and the pressure was measured using a hydrophone. Snapshots from the motion of the device are shown in Fig. 11(b) and Fig. S8 along with the measured pressure. The position was extracted using subpixel resolution image processing algorithm[62]. Plotting the displacement versus the measured pressure revealed that the beam deflection was frequency and amplitude-dependent, Fig. 12. Even though the deflections were large and extend beyond the linear beam theory (i.e., the displacement is proportional to the force), we were able to obtain a good fit for a quadratic dependency of the deflection versus the pressure, according to theory[63]. The fitted models are $x=0.8183p^2$ (R^2=0.9779) at 72.4 kHz and $x=-0.1073p^2$ (R^2=0.9965) at 127.3 kHz. Following the theoretical results in Fig. 10, larger deflections were obtained close to the first rather than the second natural frequency. The experimentally measured displacement ratio is around 13% while the theoretical maximal force ratio that is proportional to the displacement is around 19%.

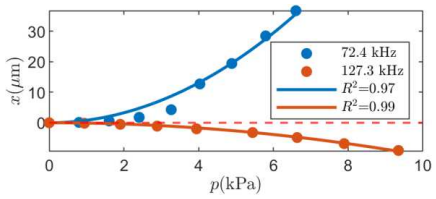

Fig. 12. The measured deflection at the beam's end at two frequencies versus the applied pressure amplitude, and the fitted curves.

VI. CONCLUSIONS

We introduced an improved model to describe the dynamics of an arbitrarily shaped microbubble with multiple circular openings. The model can simulate more accurate geometries compared to the existing models by solving an optimization problem that couples acoustics and dynamics. Once the modal parameters are known, the system's response to external pressure can be computed. Then, the resulting AS and thrust can be computed numerically by a FEM simulation. The ability to estimate the natural frequencies and vibration modes was experimentally validated for a bubble with two openings, by visualizing the streaming patterns and qualitatively estimating the thrust.

The dynamical model comprises function series, which should be truncated for computational efficiency; however, a careful convergence analysis is required. Erroneous results may be obtained if too many elements are truncated. An additional source of errors arises if in the two extreme cases (i.e., baffled and free) the order of the vibration modes is different, as discussed in Section III. Using this model, the importance of the baffle region, R, was exemplified for several cases. The baffle region has a considerable influence on the natural frequencies, as shown in Table 1 and Table 2. Because microbubble-based devices are actuated with ultrasound transducers that usually have a narrow band, matching the natural frequencies of the device and the transducer is instrumental for higher efficiency.

The conventional wisdom suggests exciting the microbubbles at their resonance frequencies to achieve good performances. Nevertheless, optimal performances are obtained when bubbles are excited at the natural frequencies, at which the interface velocity, and not displacement, is maximal. This correlates well with the fundamentals of acoustics, where the field is driven by velocity rather than displacement. An additional advantage of natural frequencies is that they are inherent characteristics of the system and are independent of dissipation. The natural frequencies and vibration modes depend on multiple parameters. Here, we only focused on geometry. We studied the vibration modes of bubbles with one and two openings, the generated streaming patterns and the thrust. It was found that lower natural frequencies were manifested by larger and more baffled bubbles (i.e., larger values of R and a). As a result, the generated thrust was also lower as thrust is highly dependent on the excitation frequency. On the other hand, it was also found that lower modes and larger bubbles are more efficient than higher modes. Therefore, selecting the optimal bubble size is not straightforward. An important yet often overlooked aspect of actuation is the excitation mechanism. It is unclear how the bubbles are excited, whether their structure is vibrated or the interface is excited by a pressure wave or both. Here, we briefly discussed the case where the interface is excited by a pressure wave and showed that if a uniform pressure is assumed only axisymmetric modes can be excited. Moreover, the latter also suggests that it should be easier and more efficient to excite mode shapes that resemble the first vibration mode of a membrane.

The loss mechanisms in general, and the modal damping in the suggested model have a crucial influence on the computed interface velocity that drives the acoustic phenomena. Estimating the modal damping is

challenging as in other physical systems, and estimating it better can lead to an improved predictive model with which the thrust and streaming patterns are computed. In Section IV, we showed only streaming patterns that are generated by a bubble with a single opening oscillating in one of the axisymmetric modes. This methodology can be simply extended for 3D configurations and general bubble oscillations.

In a rationally designed bubble with two openings, the first two vibration modes resemble with an important difference that the openings oscillate in phase or anti-phase. Also, the deflection of each interface resembles the first mode of a bubble with a single opening, thus exciting both modes is feasible. Because each mode has a distinct frequency, they are frequency-selective, and the streaming and thrust can be controlled by the excitation frequency. The complexity of the problem highlights the contribution of the suggested simplified model as a design tool for the development of advanced acoustic micromachines and manipulators.

SUPPLEMENTARY MATERIAL

See supplementary material for the video S9 showing the recorder streaming patterns generated by the bubble with two openings at different frequencies. Note 1 discusses the experimental setup that was used to measure the bubbles' interface deflection, and Note 2 provides additional information regarding the experimentally estimated deflection of the beam. Fig. S1 illustrates the experimental setup that was used to measure the bubbles' interface deflection. Fig. S2 illustrates the technique of measuring multiple locations on a microbubble using the laser Doppler vibrometer. Fig. S3 illustrates the laser beam position relative to a microbubble. Fig. S4 (a) shows the measured velocities at different locations in the water tank. Fig. S4 (b) shows the normalized measured pressure generated by the ultrasonic immersion transduces versus the frequency. Fig. S5 (a)-(c) shows the measured frequency response curves at different locations for three bubbles. Fig. S6 comprises 33 images which were used to estimate the laser beam location. Fig. S7 is a snapshot of video S7 that shows the frequency response of a bubble interface as measured at 33 locations. Fig. S8 shows the snapshots of the deflected beam that were processed to estimate its position.

ACKNOWLEDGMENTS

This project has received funding from the European Union's Horizon 2020 research and innovation programs under the European Research Council (ERC) (Grant agreement No. 714609), and under the Marie Sklodovska-Curie (Grant agreement No. 101022448). We would like to thank Theodoros Tsoulos for his assistance in the design of the optical setup, Guillermo Villanueva for generously providing the vibrometer, Izhak Bucher for fruitful discussions, EPFL Center of MicroNano Technology (CMi) staff for their technical assistance, and members of the Microbiorobotic Systems (MICROBS) Laboratory for their intellectual feedback.

DATA AVAILABILITY

The data that support the findings of this study are available from the corresponding author upon reasonable request.

CONFLICT OF INTEREST

The authors have no conflicts to disclose.

APPENDIX A

The detailed equations of the potential and kinetic energies, and the relation between a_{imn}, $b_{imn,}$ and q_{imnA} and q_{imnB} for the free and baffled bubbles are given below.

For the free bubble, the potential energy is

$$\begin{aligned}
&\mathrm{E}_p = \sum_i \Bigg\{ \frac{\pi}{2} \sum_{m=1}^{\infty}\sum_{n=1}^{\infty}\sum_{q=1}^{\infty} q_{imnA} q_{imqA} m^2 F_{imnq} + \frac{\pi}{4\alpha_i^2} \sum_{q=1}^{\infty}\sum_{n=1}^{\infty} q_{i0nA} q_{i0qA} j_{0q} j_{0n} G_{i0nq} \\
&+ \frac{\pi}{8\alpha_i^2} \sum_{m=1}^{\infty}\sum_{n=1}^{\infty}\sum_{q=1}^{\infty} \left(q_{imnA} q_{imqA} + q_{imnB} q_{imqB} \right) j_{mn} j_{mq} G_{imnq} \Bigg\} \\
&+ \kappa\lambda p_0 2\pi^2 \sum_i \sum_j \alpha_i^2 \alpha_j^2 \sum_{n=1}^{\infty}\sum_{q=1}^{\infty} q_{i0nA} q_{j0qA} \frac{J_1(j_{0n}) J_1(j_{0q})}{j_{0n} j_{0q}}, \qquad \text{(A1)} \\
&F_{imnq} = \int_0^{\alpha_i} J_m\left(j_{mq} \frac{r_i}{\alpha_i} \right) J_m\left(j_{mn} \frac{r_i}{\alpha_i} \right) \frac{1}{r_i} dr_i, \\
&G_{imnq} = \int_0^{\alpha_i} \left[J_{m-1}\left(j_{mn} \frac{r_i}{\alpha_i} \right) - J_{m+1}\left(j_{mn} \frac{r_i}{\alpha_i} \right) \right] \left[J_{m-1}\left(j_{mq} \frac{r_i}{\alpha_i} \right) - J_{m+1}\left(j_{mq} \frac{r_i}{\alpha_i} \right) \right] r_i dr_i,
\end{aligned}$$

the relations between a_{imn}, b_{imn} and q_{imnA} and q_{imnB} is

$$\dot{a}_{imn} = \dot{q}_{imnA}, \quad \dot{b}_{imn} = \dot{q}_{imnB}, \qquad \text{(A2)}$$

and the kinetic energy is

$$\mathrm{E}_k^{(F)} = \frac{\pi}{2} \sum_i \sum_{n=1}^{\infty} \frac{\alpha_i^2 J_1^2(j_{0n})}{j_{0n}} \dot{q}_{i0nA}^2 + \frac{\pi}{4} \sum_i \sum_{m=1}^{\infty}\sum_{n=1}^{\infty} \frac{\alpha_i^2 J_{m+1}^2(j_{mn})}{j_{mn}} \left[\dot{q}_{imnA}^2 + \dot{q}_{imnB}^2 \right]. \qquad \text{(A3)}$$

For the baffled bubble, the relations between a_{imn}, b_{imn} and q_{imnA} and q_{imnB} is

$$\dot{a}_{imn} \Phi_{im}(h) = \sum_{n=1}^{\infty} \frac{J_{m-1}(j_{mn}) J_m(h) j_{mn}}{h^2 - j_{mn}^2} \dot{q}_{imnA}, \quad \dot{b}_{imn} \Phi_{im}(h) = \sum_{n=1}^{\infty} \frac{J_{m-1}(j_{mn}) J_m(h) j_{mn}}{h^2 - j_{mn}^2} \dot{q}_{imnB}, \qquad \text{(A4)}$$

and the kinetic energy is

$$
\begin{aligned}
\mathrm{E}_k^{(B)} &= \pi\alpha_i^2 \sum_i \sum_{n=1}^{\infty}\sum_{q=1}^{\infty} \partial\dot{q}_{i0nA}\partial\dot{q}_{i0qA} J_{-1}\left(j_{0q}\right) J_{-1}\left(j_{0n}\right) j_{0n} j_{0q} f_{0nq} \\
&+ \frac{\pi\alpha_i^2}{2} \sum_i \sum_{m=1}^{\infty}\sum_{n=1}^{\infty}\sum_{q=1}^{\infty} \left(\dot{q}_{imnA}\dot{q}_{imqA} + \dot{q}_{imnB}\dot{q}_{imqB}\right) J_{m-1}\left(j_{mn}\right) J_{m-1}\left(j_{mq}\right) j_{mn} j_{mq} f_{mnq}, \qquad \text{(A5)} \\
f_{mnq} &= \int_0^{\infty} \frac{J_m^2(k)}{\left(k^2 - j_{mn}^2\right)\left(k^2 - j_{mq}^2\right)} dk.
\end{aligned}
$$

APPENDIX B

According to the DOF order defined in Eq.(24), the elements of the mass and stiffness matrices can be computed. The stiffness matrix is the same for both cases and is given by

$$
\mathbf{K} = \left(\begin{array}{c|c:c|c:c}
\mathbf{K}_{10} & & \mathbf{K}_{120} & & \\
\hdashline
 & \mathbf{K}_{1m} & & & \\
\hline
\mathbf{K}_{120} & & \mathbf{K}_{20} & & \\
\hdashline
 & & & \mathbf{K}_{2m} &
\end{array}\right),
$$

$$
\begin{aligned}
\left(\mathbf{K}_{10}\right)_{qn} &= \frac{\pi}{2\alpha_1^2} j_{0q} j_{0n} G_{10nq} + \kappa\lambda p_0 4\pi^2\alpha_1^4 \frac{J_1\left(j_{0n}\right) J_1\left(j_{0q}\right)}{j_{0n} j_{0q}}, \\
\left(\mathbf{K}_{1m}\right)_{qn} &= \pi m^2 F_{1mnq} + \frac{\pi}{4\alpha_1^2} j_{mn} j_{mq} G_{1mnq}, \qquad \text{(B1)} \\
\left(\mathbf{K}_{20}\right)_{qn} &= \frac{\pi}{2\alpha_2^2} j_{0q} j_{0n} G_{20nq} + \kappa\lambda p_0 4\pi^2\alpha_2^4 \frac{J_1\left(j_{0n}\right) J_1\left(j_{0q}\right)}{j_{0n} j_{0q}}, \\
\left(\mathbf{K}_{2m}\right)_{qn} &= \pi m^2 F_{2mnq} + \frac{\pi}{4\alpha_2^2} j_{mn} j_{mq} G_{2mnq}, \\
\left(\mathbf{K}_{120}\right)_{qn} &= \kappa\lambda p_0 4\pi^2\alpha_1^2\alpha_2^2 \frac{J_1\left(j_{0n}\right) J_1\left(j_{0q}\right)}{j_{0n} j_{0q}},
\end{aligned}
$$

The mass matrices for the free and baffled cases differ. For the free bubble, the mass matrix is

$$
\mathbf{M}^{(F)} = \left(\begin{array}{c|c:c|c:c}
\mathbf{M}_{10}^{(F)} & & & & \\
\hdashline
 & \mathbf{M}_{1m}^{(F)} & & & \\
\hline
 & & \mathbf{M}_{20}^{(F)} & & \\
\hdashline
 & & & \mathbf{M}_{2m}^{(F)} &
\end{array}\right),
\qquad
\begin{aligned}
\left(\mathbf{M}_{10}^{(F)}\right)_{nn} &= \frac{\pi\alpha_1^2 J_1^2\left(j_{0n}\right)}{j_{0n}}, \\
\left(\mathbf{M}_{1m}^{(F)}\right)_{nn} &= \frac{\pi\alpha_1^2 J_{m+1}^2\left(j_{mn}\right)}{2 j_{mn}}, \\
\left(\mathbf{M}_{20}^{(F)}\right)_{nn} &= \frac{\pi\alpha_2^2 J_1^2\left(j_{0n}\right)}{j_{0n}}, \\
\left(\mathbf{M}_{2m}^{(F)}\right)_{nn} &= \frac{\pi\alpha_2^2 J_{m+1}^2\left(j_{mn}\right)}{2 j_{mn}},
\end{aligned}
\qquad \text{(B2)}
$$

For the baffled bubble, the mass matrix is

$$\mathbf{M}^{(B)}=\begin{pmatrix}\mathbf{M}_{10}^{(B)} & & & \\ & \mathbf{M}_{1m}^{(B)} & & \\ & & \mathbf{M}_{20}^{(B)} & \\ & & & \mathbf{M}_{2m}^{(B)}\end{pmatrix},\qquad \begin{aligned}\left(\mathbf{M}_{10}^{(B)}\right)_{nq}&=2\pi\alpha_1^2J_{-1}\left(j_{0q}\right)J_{-1}\left(j_{0n}\right)j_{0n}j_{0q}f_{0nq},\\ \left(\mathbf{M}_{1m}^{(B)}\right)_{nq}&=\pi\alpha_1^2J_{m-1}\left(j_{mn}\right)J_{m-1}\left(j_{mq}\right)j_{mn}j_{mq}f_{mnq},\\ \left(\mathbf{M}_{20}^{(B)}\right)_{nq}&=2\pi\alpha_2^2J_{-1}\left(j_{0q}\right)J_{-1}\left(j_{0n}\right)j_{0n}j_{0q}f_{0nq},\\ \left(\mathbf{M}_{2m}^{(B)}\right)_{nq}&=\pi\alpha_1^2J_{m-1}\left(j_{mn}\right)J_{m-1}\left(j_{mq}\right)j_{mn}j_{mq}f_{mnq}.\end{aligned}\tag{B3}$$

The stiffness matrix of the intermediate case remains unchanged while the mass matrix is computed as follows.

$$\begin{aligned}\mathbf{M}^{(I)}=&\begin{pmatrix}\mathrm{e}^{-\beta_1(R_1-\alpha_1)}\mathbf{M}_{10}^{(F)} & & & \\ & \mathrm{e}^{-\beta_1(R_1-\alpha_1)}\mathbf{M}_{1m}^{(F)} & & \\ & & \mathrm{e}^{-\beta_2(R_2-\alpha_2)}\mathbf{M}_{20}^{(F)} & \\ & & & \mathrm{e}^{-\beta_2(R_2-\alpha_2)}\mathbf{M}_{2m}^{(F)}\end{pmatrix}\\ &+\begin{pmatrix}\left(1-\mathrm{e}^{-\beta_1(R_1-\alpha_1)}\right)\mathbf{M}_{10}^{(B)} & & & \\ & \left(1-\mathrm{e}^{-\beta_1(R_1-\alpha_1)}\right)\mathbf{M}_{1m}^{(B)} & & \\ & & \left(1-\mathrm{e}^{-\beta_2(R_2-\alpha_2)}\right)\mathbf{M}_{20}^{(B)} & \\ & & & \left(1-\mathrm{e}^{-\beta_2(R_2-\alpha_2)}\right)\mathbf{M}_{2m}^{(B)}\end{pmatrix}.\end{aligned}\tag{B4}$$

References

[1] Y. Li, X. Liu, Q. Huang, A.T. Ohta, and T. Arai, Lab Chip (2021).

[2] D. Ahmed, A. Ozcelik, N. Bojanala, N. Nama, A. Upadhyay, Y. Chen, W. Hanna-Rose, and T.J. Huang, Nat. Commun. **7**, 1 (2016).

[3] A. Aghakhani, O. Yasa, P. Wrede, and M. Sitti, Proc. Natl. Acad. Sci. U. S. A. **117**, 3469 (2020).

[4] L. Ren, N. Nama, J.M. McNeill, F. Soto, Z. Yan, W. Liu, W. Wang, J. Wang, and T.E. Mallouk, Sci. Adv. **5**, eaax3084 (2019).

[5] D. Ahmed, M. Lu, A. Nourhani, P.E. Lammert, Z. Stratton, H.S. Muddana, V.H. Crespi, and T.J. Huang, Sci. Rep. **5**, (2015).

[6] S. Boluriaan and P.J. Morris, Int. J. Aeroacoustics **2**, 255 (2003).

[7] N. Riley, Annu. Rev. Fluid Mech. **33**, 43 (2001).

[8] T. Leighton, *The Acoustic Bubble* (Academic Press, 2012).

[9] N. Bertin, T.A. Spelman, O. Stephan, L. Gredy, M. Bouriau, E. Lauga, and P. Marmottant, Phys. Rev. Appl. **4**, 064012 (2015).

[10] T.A. Spelman, O. Stephan, and P. Marmottant, Ultrasonics **102**, 106054 (2020).

[11] A. Volk and C.J. Kähler, Phys. Rev. Appl. **9**, 054015 (2018).

[12] R. Bolaños-Jiménez, M. Rossi, D.F. Rivas, C.J. Kähler, and A. Marin, J. Fluid Mech. **820**, 529 (2017).

[13] C. Wang, B. Rallabandi, and S. Hilgenfeldt, Phys. Fluids **25**, 022002 (2013).

[14] I. Turmo De Arcos Gonzalez, Forcing Microbubbles in Microfluidics, Universidad de Sevilla, 2019.

[15] T. Luo and M. Wu, Lab Chip (2021).

[16] A. Dolev, M. Kaynak, and M.S. Sakar, Adv. Intell. Syst. 2000233 (2021).

[17] G. Regnault, C. Mauger, P. Blanc-Benon, A.A. Doinikov, and C. Inserra, J. Acoust. Soc. Am. **150**, 1188 (2021).

[18] Y. Hao, Y. Zhang, and A. Prosperetti, Phys. Rev. Fluids **2**, 034303 (2017).

[19] M. Versluis, S.M. Van Der Meer, D. Lohse, P. Palanchon, D. Goertz, C.T. Chin, and N. De Jong, in *Proc. - IEEE Ultrason. Symp.* (2004), pp. 207–209.

[20] D. V. Lyubimov, T.P. Lyubimova, and A.A. Cherepanov, J. Fluid Mech. **909**, 18 (2020).

[21] V. V. Konovalov, D. V. Lyubimov, and T.P. Lyubimova, Phys. Fluids **33**, 094107 (2021).

[22] H.K. Hassan and Y.A. Stepanyants, Phys. Fluids **29**, 101703 (2017).

[23] M. De Corato, B. Saint-Michel, G. Makrigiorgos, Y. Dimakopoulos, J. Tsamopoulos, and V. Garbin, Phys. Rev. Fluids **4**, 073301 (2019).

[24] D.B. Khismatullin and A. Nadim, Phys. Fluids **14**, 3534 (2002).

[25] Q.X. Wang, Phys. Fluids **29**, 072101 (2017).

[26] J. Loughran, R.J. Eckersley, and M.-X. Tang, J. Acoust. Soc. Am. **131**, 4349 (2012).

[27] A.J. Sojahrood, H. Haghi, T.M. Porter, R. Karshafian, and M.C. Kolios, Phys. Fluids **33**, 072006 (2021).

[28] A. Maksimov, Phys. Fluids **32**, 102104 (2020).

[29] D.L. Miller and W.L. Nyborg, J. Acoust. Soc. Am. **73**, 1537 (1983).

[30] H. Gelderblom, A.G. Zijlstra, L. van Wijngaarden, and A. Prosperetti, Phys. Fluids **24**, 122101 (2012).

[31] D. Gritsenko, Y. Lin, V. Hovorka, Z. Zhang, A. Ahmadianyazdi, and J. Xu, Phys. Fluids **30**, 082001 (2018).

[32] C. Chindam, N. Nama, M. Ian Lapsley, F. Costanzo, and T. Jun Huang, J. Appl. Phys. **114**, 194503 (2013).

[33] O. Schnitzer, R. Brandão, and E. Yariv, Phys. Rev. B **99**, 195155 (2019).

[34]Artificial Micro-Devices: Armoured Microbubbles and a Magnetically Driven Cilium, University of Cambridge, 2017.

[35] M. Harazi, M. Rupin, O. Stephan, E. Bossy, and P. Marmottant, Phys. Rev. Lett. **123**, 254501 (2019).

[36] M. Boughzala, O. Stephan, E. Bossy, B. Dollet, and P. Marmottant, Phys. Rev. Lett. **126**, 054502 (2021).

[37] M. Minnaert, London, Edinburgh, Dublin Philos. Mag. J. Sci. **16**, 235 (1933).

[38] A. Dolev, S. Davis, and I. Bucher, Phys. Rev. Appl. **12**, 034031 (2019).

[39] P.B. Muller, R. Barnkob, M.J.H. Jensen, and H. Bruus, Lab Chip **12**, 4617 (2012).

[40] B. Behdani, S. Monjezi, J. Zhang, C. Wang, and J. Park, Korean J. Chem. Eng. **37**, 2117 (2020).

[41] D.J. Ewins, *Modal Testing: Theory, Practice, and Application* (Research Studies Press, 2000).

[42] J.T. Karlsen and H. Bruus, Phys. Rev. E - Stat. Nonlinear, Soft Matter Phys. **92**, 043010 (2015).

[43] G. Zhou and A. Prosperetti, J. Fluid Mech. **901**, 3 (2020).

[44] G. Zhou, J. Acoust. Soc. Am. **149**, 923 (2021).

[45] Y.Q. Yu and Z. Zong, Phys. Fluids **33**, 076106 (2021).

[46] H. Lamb, *Hydrodynamics*, 6th ed. (Dover publications, 1945).

[47] S.S. Rao, *Vibration of Continuous Systems*, 2nd ed. (John Wiley & Sons, 2019).

[48] J.Y. Chang and J.A. Wickert, J. Sound Vib. **242**, 69 (2001).

[49] R. Gabai, D. Ilssar, R. Shaham, N. Cohen, and I. Bucher, Sensors Actuators, A Phys. **255**, 34 (2017).

[50] V. Cutanda Henriquez and P.M. Juhl, in *Internoise 2010* (Lisbon, 2010), pp. 5796–5805.

[51] M.F. Hamilton and D.T. Blackstock, *Nonlinear Acoustics* (Academic Press, 1998).

[52] S.J. Kleis and L.A. Sanchez, Sol. Energy **45**, 201 (1990).

[53] W.M. Haynes, D.R. Lide, and T.J. Bruno, *CRC Handbook of Chemistry and Physics*, 97th ed. (CRC Press, Taylor & Francis Group, 2016).

[54] A.A. Doinikov, *Bubble and Particle Dynamics in Acoustic Fields: Modern Trends and Applications* (Research Signpost, 2005).

[55] Z.L. Tian, Y.L. Liu, A.M. Zhang, and L. Tao, Ocean Eng. **196**, 106714 (2020).

[56] W. Lauterborn and T. Kurz, Reports Prog. Phys. **73**, 106501 (2010).

[57] A.J. Sojahrood, H. Haghi, R. Karshafian, and M.C. Kolios, Phys. Fluids **33**, 016105 (2021).

[58] M. Kaynak, P. Dirix, and M.S. Sakar, Adv. Sci. 2001120 (2020).

[59] N. Bertin, T.A. Spelman, O. Stephan, L. Gredy, M. Bouriau, E. Lauga, and P. Marmottant, Phys. Rev. Appl. **4**, 064012 (2015).

[60] J. Feng, J. Yuan, and S.K. Cho, Lab Chip **15**, 1554 (2015).

[61] M. Hippler, K. Weißenbruch, K. Richler, E.D. Lemma, M. Nakahata, B. Richter, C. Barner-Kowollik, Y. Takashima, A. Harada, E. Blasco, M. Wegener, M. Tanaka, and M. Bastmeyer, Sci. Adv. **6**, (2020).

[62] M. Guizar-Sicairos, S.T. Thurman, and J.R. Fienup, Opt. Lett. **33**, 156 (2008).

[63] H. Bruus, Lab Chip **12**, 1578 (2012).

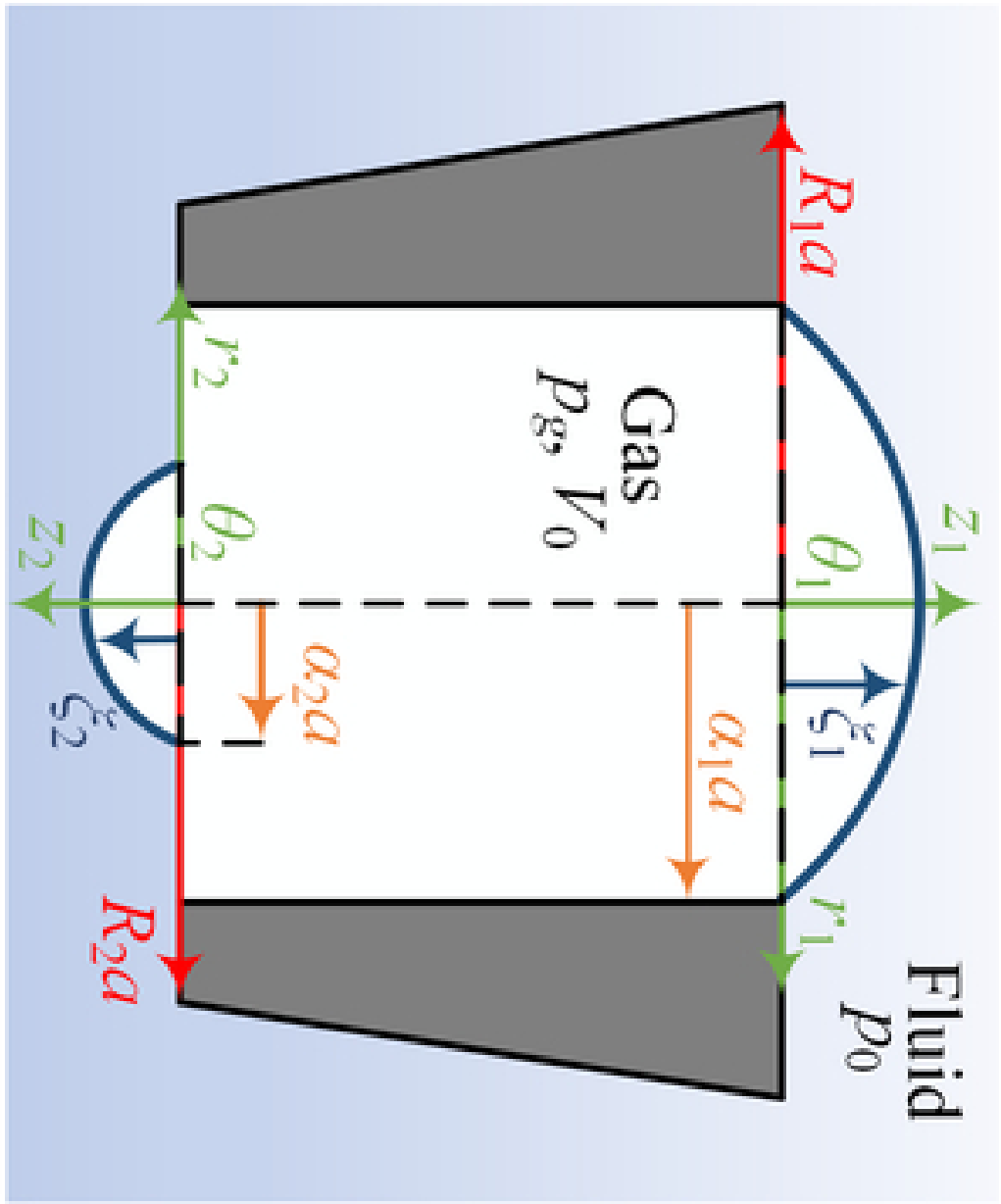

PLEASE CITE THIS ARTICLE AS DOI: 10.1063/5.0075876

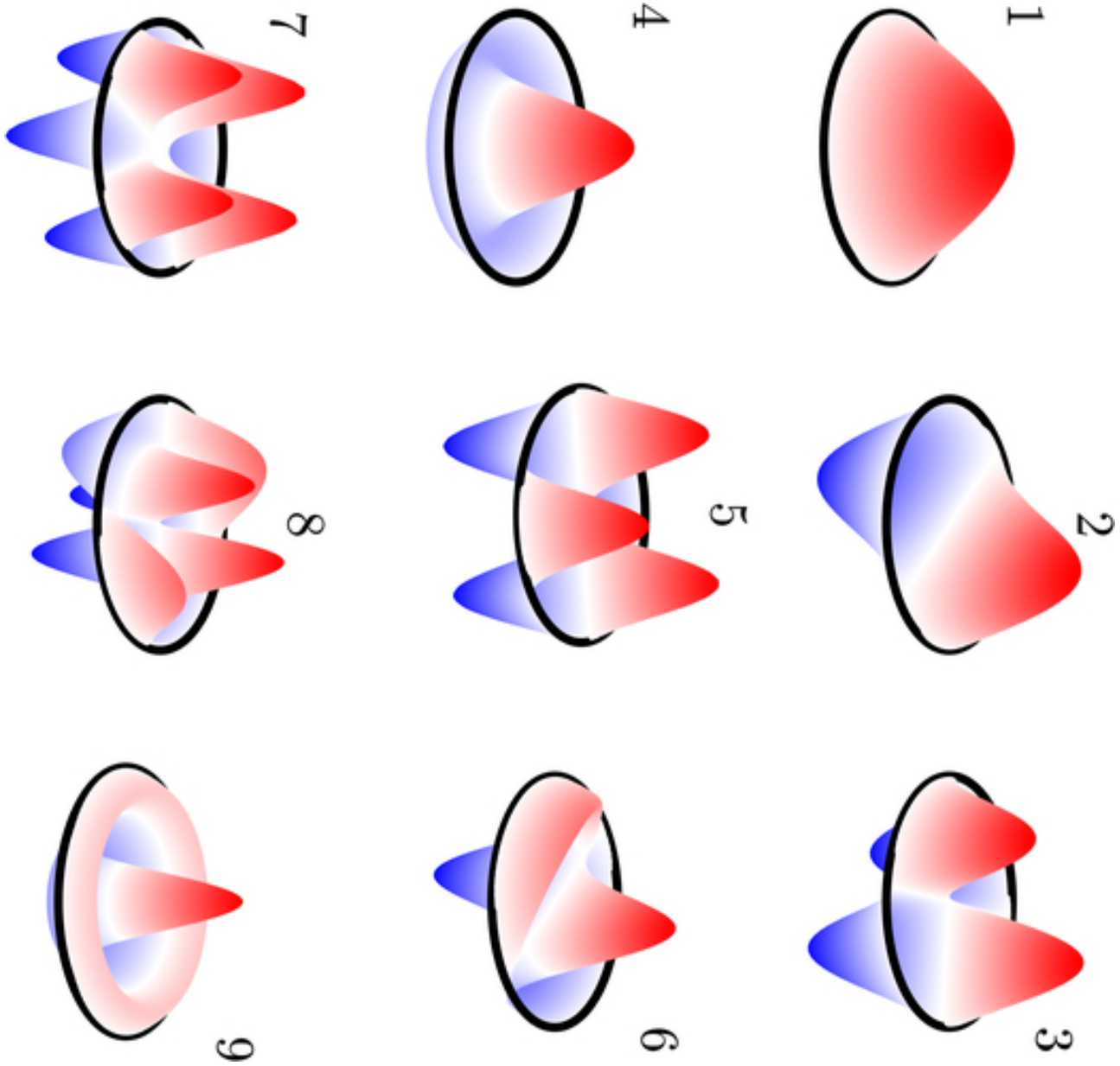

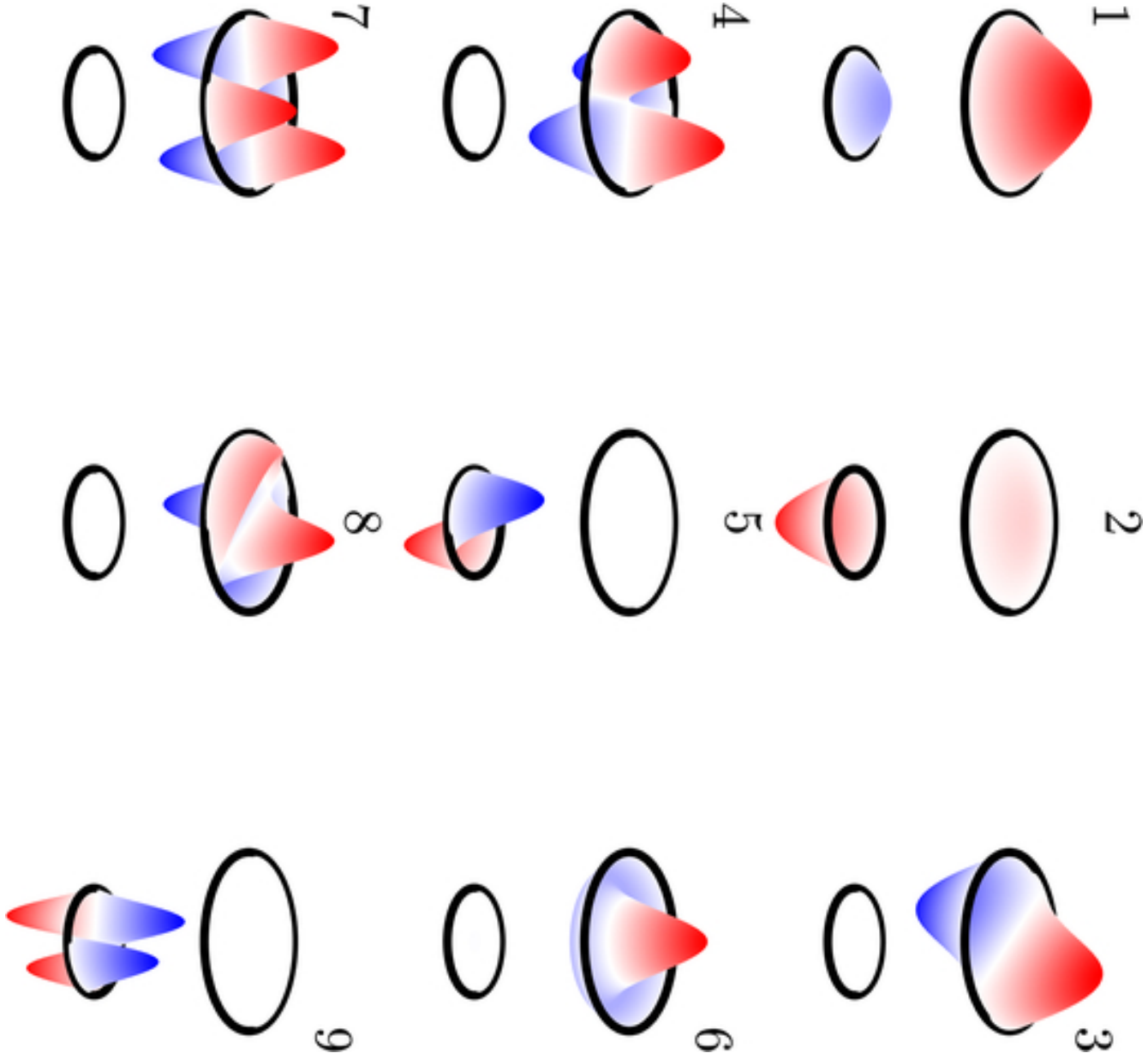

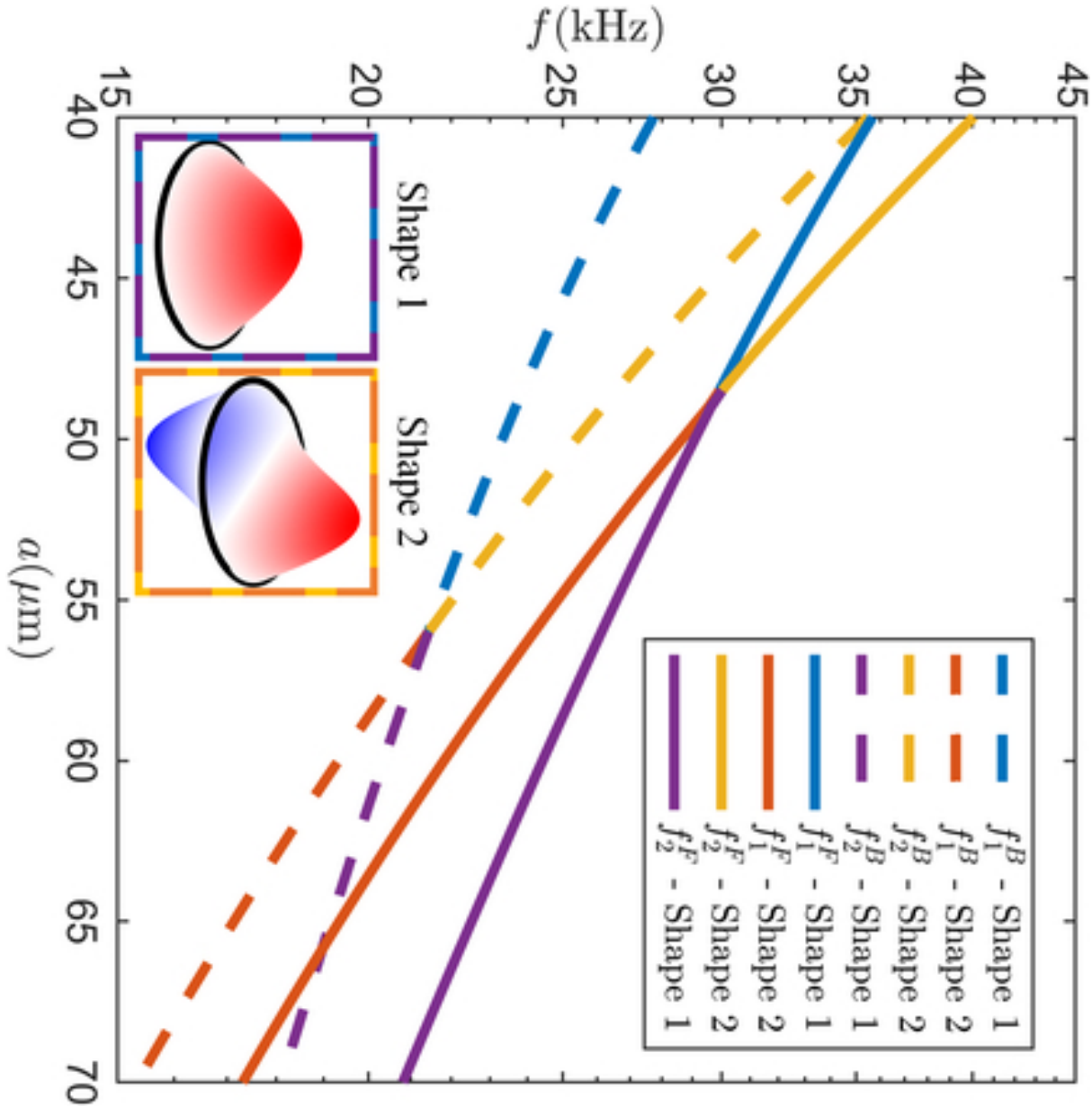

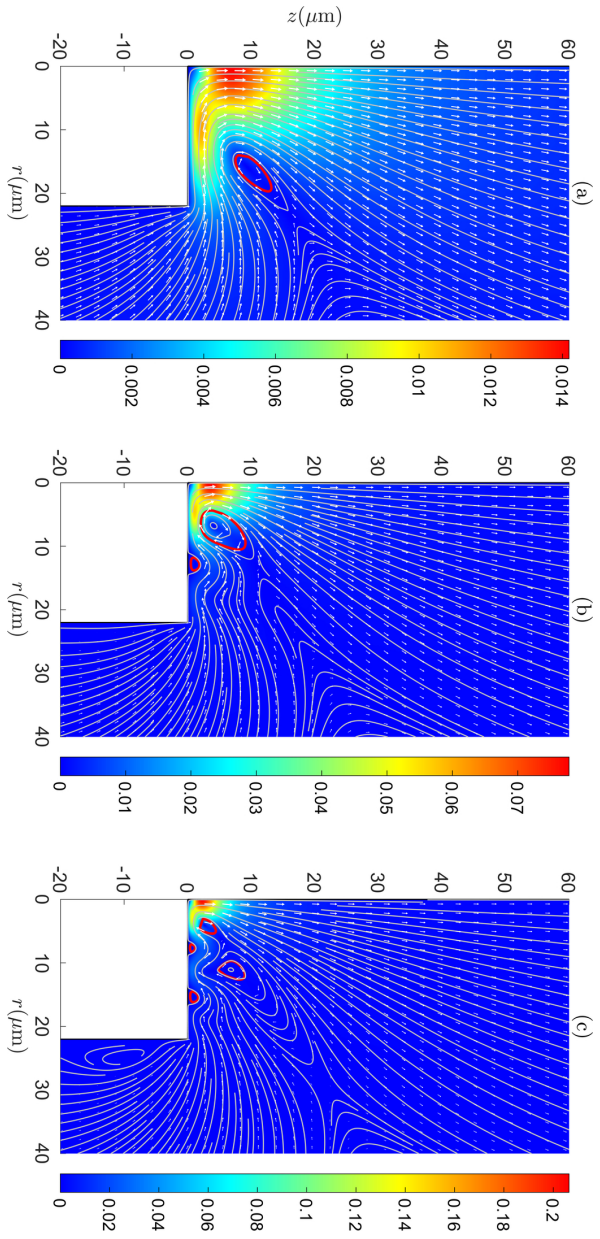

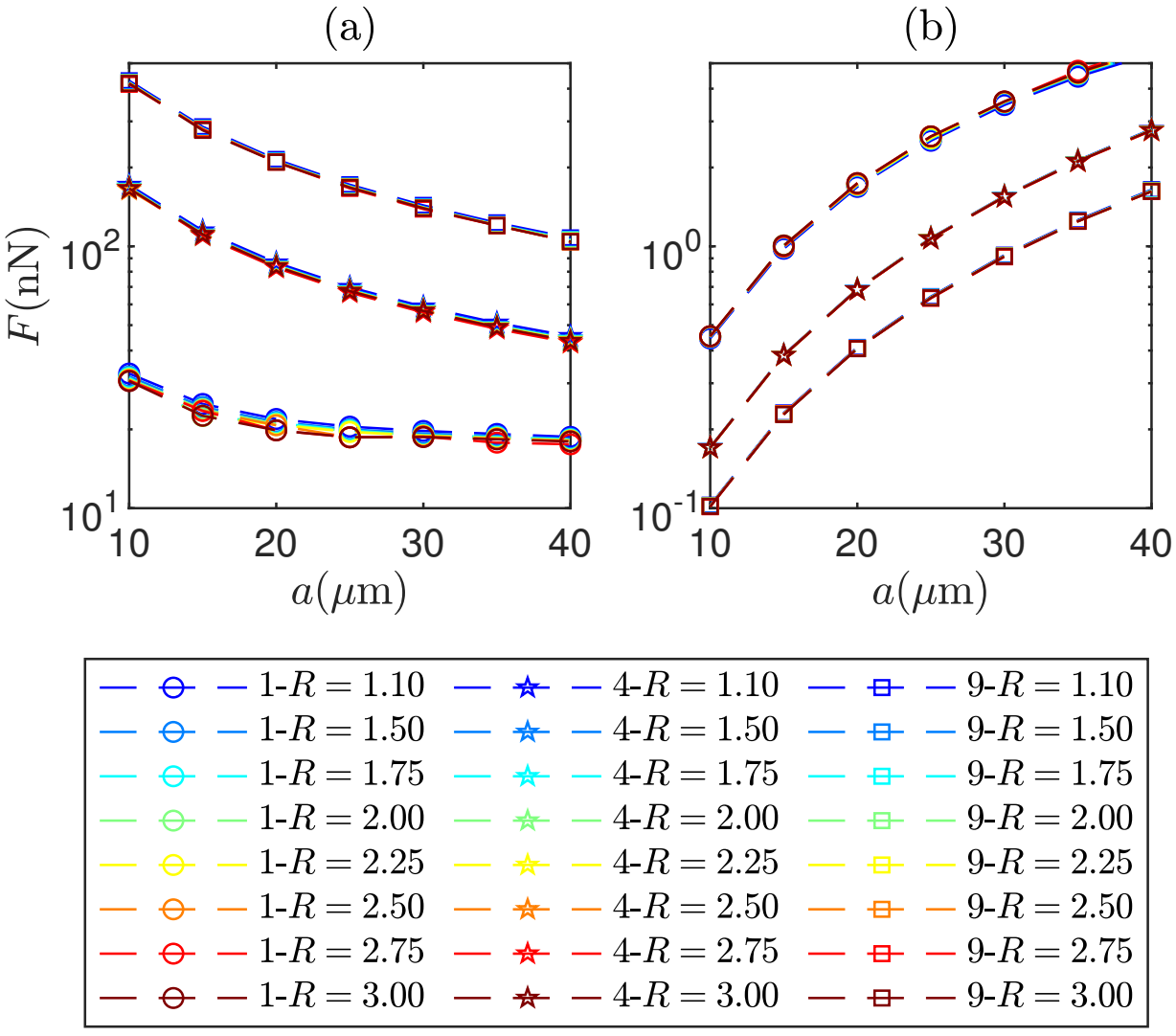

PLEASE CITE THIS ARTICLE AS DOI: 10.1063/5.0075876

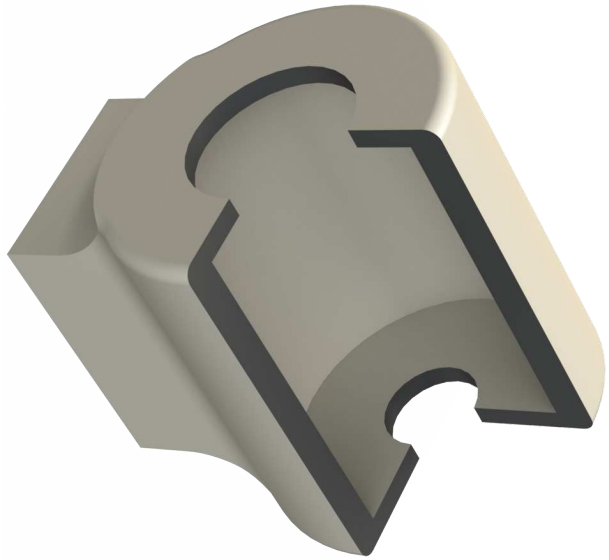

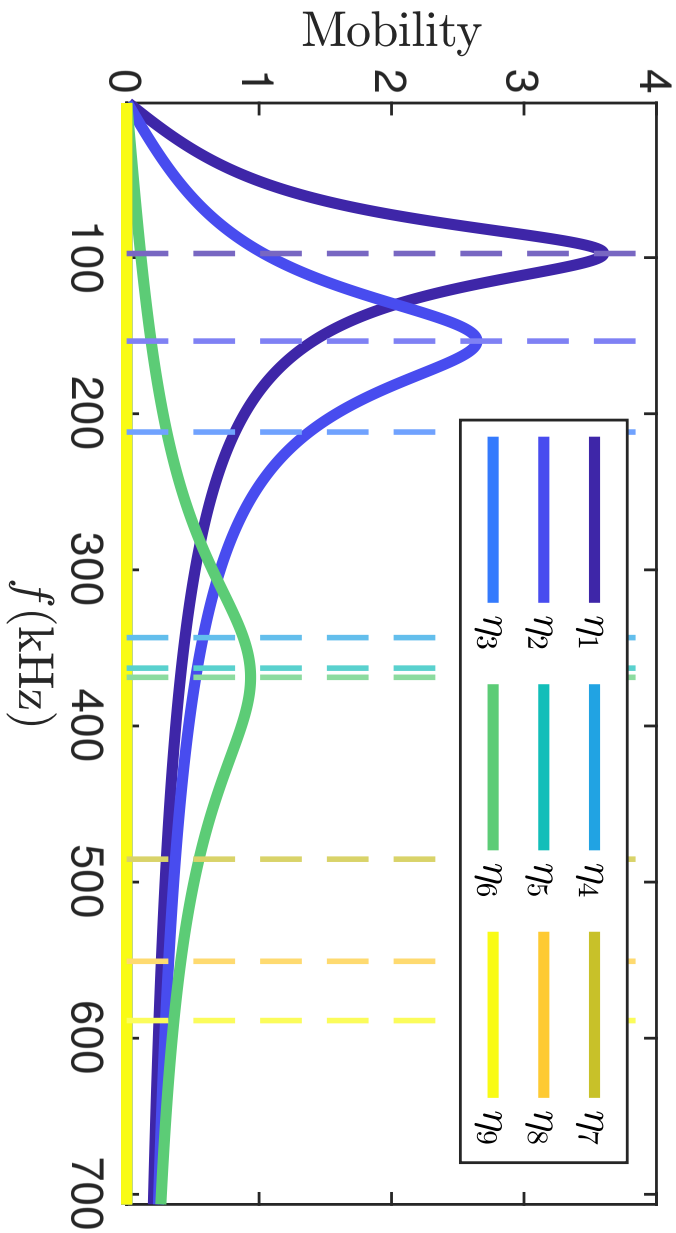

PLEASE CITE THIS ARTICLE AS DOI: 10.1063/5.0075876